npj | materials degradation

Article

Published in partnership with CSCP and USTB

https://doi.org/10.1038/s41529-024-00455-9

Investigation on improving the comprehensive performance of environmental barrier coating materials by high-entropy multiphase design

Zeyu Chen[1,2], Yongzhe Wang[1] ✉, Yiling Huang[1], Fan Peng[1], Chucheng Lin[1], Wei Zheng[1], Xuemei Song[1], Yaran Niu[3] & Yi Zeng[1] ✉

It is difficult to obtain a single-phase environmental barrier coating material that simultaneously offers the advantages of low thermal conductivity, a suitable coefficient of thermal expansion, and excellent corrosion resistance. Herein, to synthesize the advantages of single-phase materials, we have developed an effective approach for the design of high-entropy multiphase ceramics of rare earth oxides and silicates. Such a specific design approach is capable of making high-entropy RE_2SiO_5/RE_2O_3 and RE_2SiO_5/$RE_2Si_2O_7$ (RE = Lu, Yb, Tm, Er, Ho, and Y) multiphase ceramics as two types of potential environmental barrier coating materials for Al_2O_{3f}/Al_2O_3 and SiC_f/SiC ceramic matrix composites.

Ceramic matrix composites (CMCs) are suitable materials to replace nickel-based alloys in aero-engine hot-end components[1–3]. Among them, SiC_f/SiC and Al_2O_{3f}/Al_2O_3 composites are up-to-date candidates with excellent mechanical properties, low density, and high-temperature phase stability[4–6]. However, in the environment of the combustion chamber, corrosive media such as water vapor produced during fuel combustion and calcium–magnesium aluminosilicate (CMAS) molten salt corrode the substrate[7–10]. These corrosive behaviors restrict the widespread application of SiC_f/SiC and Al_2O_{3f}/Al_2O_3 composites. An effective way to solve these problems is to cover the surface of CMCs with environmental barrier coatings (EBCs) to prevent corrosive media from affecting them[11–13].

Due to the high melting point of Y_2O_3 (approximately 2500 °C)[14] and its closely matched thermal expansion coefficient (CTE; 8.6–9.6 × 10^{-6} K^{-1})[15,16] to that of Al_2O_3 (8.5–9.0 × 10^{-6} K^{-1})[17], previous investigations have revealed that Y_2O_3 exhibits significant promise as an EBC material. Nevertheless, the high thermal conductivity (21.4 W m^{-1} K^{-1} at 300 °C)[13] at low-temperature ranges and unsatisfactory resistance to CMAS corrosion make Y_2O_3 fall short of meeting the service requirements[18]. To alleviate the thermal conductivity of Y_2O_3, several high-entropy rare earth (RE) oxides have been designed in the past few years[13,19]. The enhanced phonon scattering caused by the combined compositional disorder and strong lattice distortion leads to a certain degree of thermal conductivity reduction[20]. In addition, due to the suitable coefficients of thermal expansion, some other ceramic systems obtained by high-entropy design, such as high-entropy aluminate[21,22], and high-entropy phosphate[23,24], are also suitable for Al_2O_{3f}/Al_2O_3 composite. However, there is a scarcity of reports regarding the CMAS corrosion resistance of these innovative high-entropy single-phase materials. Hence, the availability of low thermal conductivity, a CTE that matches Al_2O_{3f}/Al_2O_3 composite, and strong corrosion resistance all at the same time remains a formidable challenge for single-phase materials.

X2-type RE monosilicates (X2-RE_2SiO_5) with excellent corrosion resistance are the preferred environmental barrier coating materials for SiC_f/SiC composites, and their thermal conductivity can also be reduced via a well-designed high-entropy approach[25,26]. For instance, the thermal conductivity of four-component monosilicate—$(Ho_{1/4}Lu_{1/4}Yb_{1/4}Eu_{1/4})_2SiO_5$ at 200 °C is only 1.47 W m^{-1} K^{-1}[3]. However, the CTEs of most X2-type monosilicates are approximately 6.0–7.8 × 10^{-6} k^{-1} at 1400 °C[27]. Such a CTE range does not match that of SiC_f/SiC CMC (4.5–5.9×10^{-6} K^{-1})[28]. During the thermal cycling process, the challenge of coating delamination persists due to the mismatched CTEs in the application of monosilicates. The CTEs of β-type RE pyrosilicates ($RE_2Si_2O_7$; 4.0–5.4×10^{-6} K^{-1})[29] are very close to that of the SiC_f/SiC CMC and Si bonding layer[30], coatings prepared by these

[1]The State Key Lab of High Performance Ceramics and Superfine Microstructure, Shanghai Institute of Ceramics, Chinese Academy of Sciences, Shanghai 200050, China. [2]Center of Materials Science and Optoelectronics Engineering, University of Chinese Academy of Sciences, 100049 Beijing, China. [3]Key Laboratory of Inorganic Coating Materials CAS, Shanghai Institute of Ceramics, Chinese Academy of Sciences, Shanghai 200050, China.
✉e-mail: wangyongzhe@mail.sic.ac.cn; zengyi@mail.sic.ac.cn

materials exhibit excellent thermal shock resistance[31]. Nevertheless, the high thermal conductivity and poor corrosion resistance of pyrosilicates limit their vast applications[12].

Addressing the current challenges in the application of single-phase materials, the main approach of this study is the design of high-entropy multiphase materials. This kind of multiphase design relies on mixing rules to harmonize various aspects of material's properties. On the one hand, by harmonizing the properties of RE monosilicates and RE oxides, it was desired to obtain a coating material with excellent CMAS corrosion resistance while ensuring that the coefficient of thermal expansion is between that of monosilicates and oxides and matches Al_2O_{3f}/Al_2O_3; On the other hand, by harmonizing the properties of RE monosilicates and RE pyrosilicates, it is hoped to obtain a multiphase material that can be used in SiC_f/SiC composites with a coefficient of thermal expansion that is close to β-pyrosilicates and an excellent CMAS corrosion resistance close to that of monosilicates. Simultaneously, we aim to reduce the thermal conductivity of both multiphase materials through high-entropy design. In order to ensure that the monosilicates are of type X2 and the pyrosilicates are of phase β, five rare-earth elements among lanthanide elements with the smallest ionic radius, as well as Y element with a similar ionic radius, were selected.

By modulating the ratio of RE_2O_3 to SiO_2 (0.5–1.0–1.5–2.0), the phase compositions of high-entropy ceramics are capable of undergoing the following transformations: RE_2SiO_5/RE_2O_3–RE_2SiO_5–$RE_2SiO_5/RE_2Si_2O_7$–$RE_2Si_2O_7$. These two types of high-entropy multiphase ceramics (RE_2SiO_5/RE_2O_3 and $RE_2SiO_5/RE_2Si_2O_7$; RE = Lu, Yb, Tm, Er, Ho, and Y) were prepared by a solid-phase method in the present work. Additionally, two types of high-entropy single-phase silicate ceramics (RE_2SiO_5 and $RE_2Si_2O_7$; RE = Lu, Yb, Tm, Er, Ho, and Y) were also prepared as controls. This investigation compares the thermophysical properties and corrosion behavior of four types of high-entropy ceramics after exposure to CMAS deposition at 1,400 °C for 20 h. The results indicate that both high-entropy multiphase materials exhibit outstanding overall performance. These findings are of great advantage to further accelerate the screening process of candidate EBC materials in the presence of a broad range of conditions and provide a solid foundation for the application of EBCs to protect Al_2O_{3f}/Al_2O_3 and SiC_f/SiC composites.

Results

Phase structure and composition of four high-entropy ceramic blocks

The XRD patterns of four types of high-entropy ceramics are illustrated in Fig. 1. RES0.5 exhibited the peaks of X2-type monosilicate with space group $C2/c$ and RE oxide with space group $Ia\bar{3}$, which matched the PDF#40-0384 and PDF#08-0050 cards, as demonstrated in Fig. 1a. The X-ray diffraction analysis results were refined via the Fullprof software. The phase contents, lattice parameters (a, b, c, and β), and measured densities obtained for the four types of high-entropy ceramics are presented in Table 1. The ratio of the phase content of RE_2SiO_5 to RE_2O_3 in RES0.5 is close to 1:1. The diffraction peaks of RES1.0 and RES2.0 corresponded to PDF cards of PDF#40-0384 and PDF#25-1345, as presented in Figs. 1b and 1d, exhibited the X2-type monosilicate single phase with space group $C2/c$ and β-type pyrosilicate single phase with space group $C2/m$, respectively. However, RES1.5 showed multiphase peaks of X2-type monosilicate and β-type pyrosilicate, as shown in Fig. 1c, and the phase content ratios of these two phases in RES1.5 are also close to 1:1.

Figure 1a illustrates the schematic crystal structure of RE_2O_3. The high-entropy RE^{3+} is located at 8a (1/4, 1/4, 1/4) (seven-coordination) and 24d (x, 0, 1/4) sites (seven-coordination), while O atoms occupy the 48e (x,y,z) sites. The unit cell of X2-RE_2SiO_5 contains 32 atoms (Fig. 1a–c), with RE^{3+} occupying two unequal positions, including Site 1 $[REO_7]^{11-}$ (seven coordination) and Site 2 $[REO_6]^{9-}$ (six-coordination). The Si atoms occupy one position and form a $[SiO_4]^{4-}$ tetrahedron with four adjacent oxygen atoms. According to β-type pyrosilicate structures (Fig. 1c, d), RE^{3+} is bonded to six adjacent oxygen atoms, whereas Si atoms are bonded to four adjacent oxygen atoms. In addition, the corresponding crystal consists of $[Si_2O_7]^{6-}$ units and RE^{3+} stacked along the b-axis. The $[Si_2O_7]^{6-}$ unit consists of two $[SiO^4]^{4-}$ tetrahedra, which are connected at the top corners.

As demonstrated in Fig. 1a–c and Table 1, although monosilicate phases are contained in all three high-entropy ceramics, there are still slight differences in lattice parameters, RE-O bond lengths of the $[REO_6]^{9-}$ polyhedral and $[REO_7]^{11-}$ polyhedra, and Si-O bond lengths of $[SiO_4]^{4-}$ polyhedra due to subtle differences in chemical compositions. A similar phenomenon exists for existing pyrosilicates in RES1.5 and RES2.0.

The surface morphology, EDS elemental mappings, and EDS semi-quantitative analysis of four types of high-entropy ceramics are presented in Fig. 2. We found that the distribution of various rare earth elements (REEs) in microns is very uniform. There exist two phases with various contrasts in the BSE images and lightness in the Si elemental mappings for RES0.5 and RES1.5 and only one phase for RES1.0 and RES2.0. Based on the semi-quantitative EDS analysis of points 1–6, it can be determined that substances at points 1, 3, and 4 are monosilicates, substance at point 2 is oxide, and substances at points 5 and 6 are pyrosilicates.

Among them, no significant differences in the contents of REEs are observed in the two phases of RES1.5. However, in RES0.5, the REE content shows an increasing trend in the oxide phase and a decreasing trend in the monosilicate phase as the ionic radius of RE^{3+} decreases. For RE cations, a larger coordination number usually corresponds to an increased open space around them. Therefore, RE^{3+} with a larger ionic radius is likely to occupy Site 1 $[REO_7]^{9-}$ (seven-coordination) of monosilicates, which possesses a larger space and leads to the aforementioned subtle elemental differences[25].

Four polished sections of high-entropy ceramic blocks were tested by EBSD to obtain the crystallographic information of the blocks, as illustrated in Fig. 3. The grains of different phases with various sizes bonded tightly together to form dense blocks of RES0.5 and RES1.5, as presented in Fig. 3a, c. Even though both XRD and SEM results indicate that RES1.0 is a single-phase monosilicate, a β-type pyrosilicate phase of less than 1% was observed in the EBSD results, as shown in Fig. 3b. This may be due to the slightly excessive Si content that led to the formation of a small amount of pyrosilicate as a heterogeneous phase during the reaction. Most of the pyrosilicate grains in RES1.5 (see Fig. 3c) and RES2.0 (see Fig. 3d) are available as twinned crystals, but most of the RES2.0 grains are columnar crystals and their grain size is much larger than the former (RES1.5). The high-entropy ceramics prepared by pressureless sintering did not show a crystal texture, as presented in the IPF Y maps of Fig. 3a–d.

Thermal performance of four high-entropy ceramic blocks

The thermal diffusivity (α), specific heat (C_p), and thermal conductivity (k) calculated using Eq. (1) of four high-entropy ceramic blocks are presented in Fig. 4. These four types of blocks showed a similar trend. As the temperature increases, the specific heat increases, while the thermal diffusivity decreases. The thermal conductivity of six-component RES1.0 at 200 °C was 1.15 $W\,m^{-1}\,K^{-1}$, which was only 47.7% of the thermal conductivity of single-component monosilicate—Lu_2SiO_5 (2.41 $W\,m^{-1}\,K^{-1}$)[25]. Due to the presence of 50% of the six-component monosilicate phase in RES0.5 and RES1.5, their thermal conductivity is remarkably lower than the reported thermal conductivities of RE oxides[13] and RES2.0.

The coefficients of thermal expansion of RES0.5, RES1.0, RES1.5, and RES2.0 from 200 °C to 1400 °C are $6.57–8.23 \times 10^{-6}$ K^{-1}, $4.81–6.59 \times 10^{-6}$ K^{-1} [25], $3.23–5.16 \times 10^{-6}$ K^{-1}, and $3.17–3.83 \times 10^{-6}$ K^{-1} [29], respectively. The CTE of RES1.5 is between those of RES1.0 and RES2.0 and is only slightly higher than RES2.0, which is close to and slightly lower than that of SiC_f/SiC ($4.5–5.9 \times 10^{-6}$ K^{-1})[28]. The CTE of another high-entropy multiphase ceramic—RES0.5 is also between that of RES1.0 and the reported CTEs of RE oxides[15,16] and is also slightly lower than that of Al_2O_{3f}/Al_2O_3 ($8.5–9.0 \times 10^{-6}$ K^{-1})[17].

CMAS corrosion resistance of four high-entropy ceramic blocks

Figure 5 illustrates the CMAS corrosion of RES0.5 at 1400 °C for 20 h. The plotted results reveal that the diffraction on the block surface is mainly apatite (corrosion product), and some monosilicate and

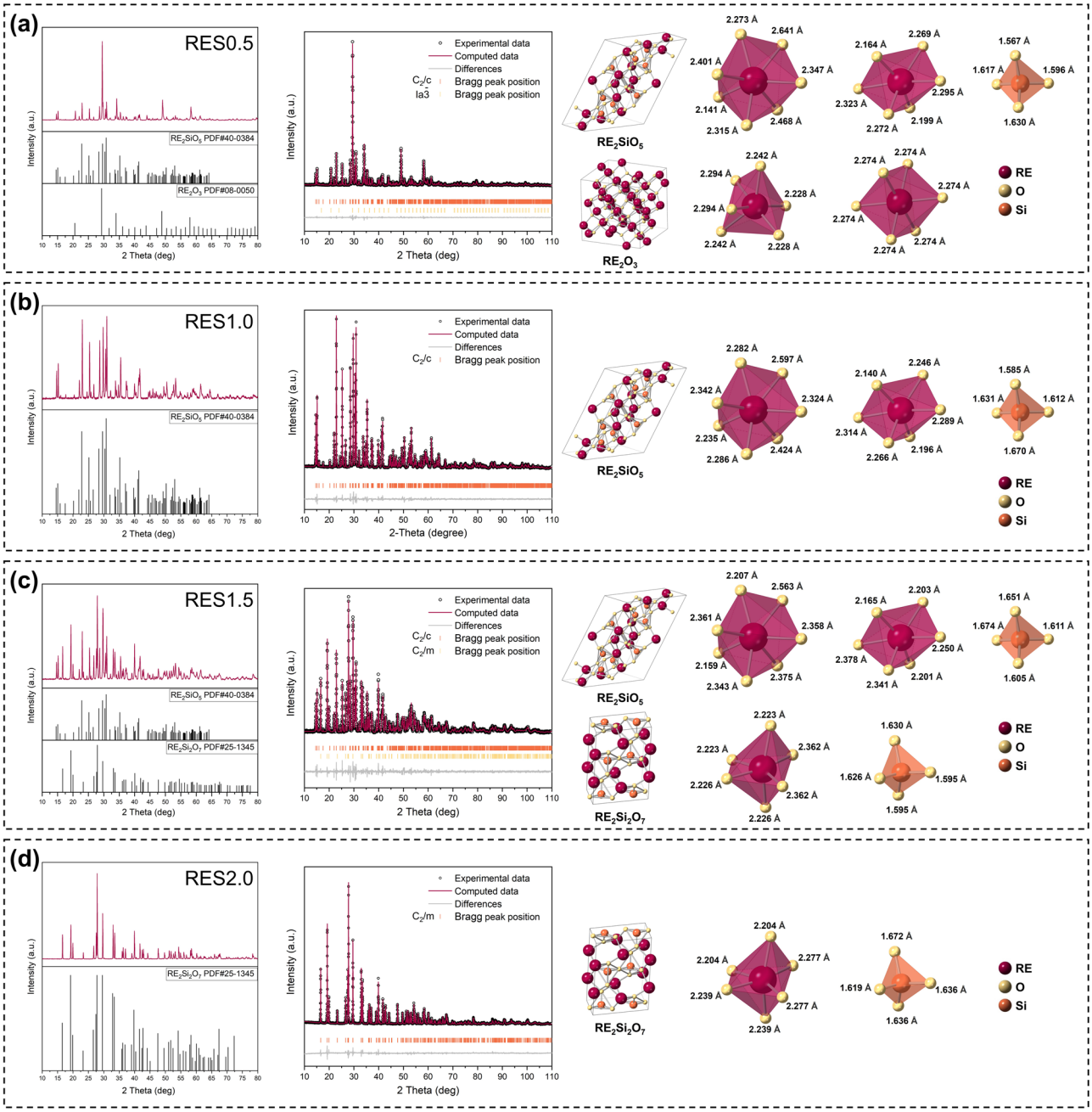

Fig. 1 | XRD patterns, Rietveld refinement of XRD patterns, crystal structure, RE-O and Si-O bond lengths of four high-entropy ceramic blocks. a RES0.5, **b** RES1.0[25], **c** RES1.5, and **d** RES2.0[29].

Table 1 | Phase contents and crystal lattice parameters obtained by the XRD Rietveld refinement and the measured densities of RES0.5, RES1.0[25], RES1.5, and RES2.0[29]

Compounds	R_P(%)	R_{WP}(%)	Phases	Contents (wt%)	a(Å)	b(Å)	c(Å)	β(°)	Measured density (g/cm³)
REO0.5	2.34	2.99	RE_2SiO_5	52.01%	14.3438	6.6941	10.3562	122.182	6.97
			RE_2O_3	47.99%	10.5034	--	--	--	
REO1.0	2.54	3.50	RE_2SiO_5	100.00%	14.3421	6.6894	10.3466	122.182	6.13
REO1.5	2.95	3.97	RE_2SiO_5	44.24%	14.3262	6.6923	10.3543	122.133	5.97
			$RE_2Si_2O_7$	55.76%	6.8312	8.9115	4.7128	101.832	
REO2.0	3.30	4.26	$RE_2Si_2O_7$	100.00%	6.8322	8.9131	4.7119	101.841	5.61

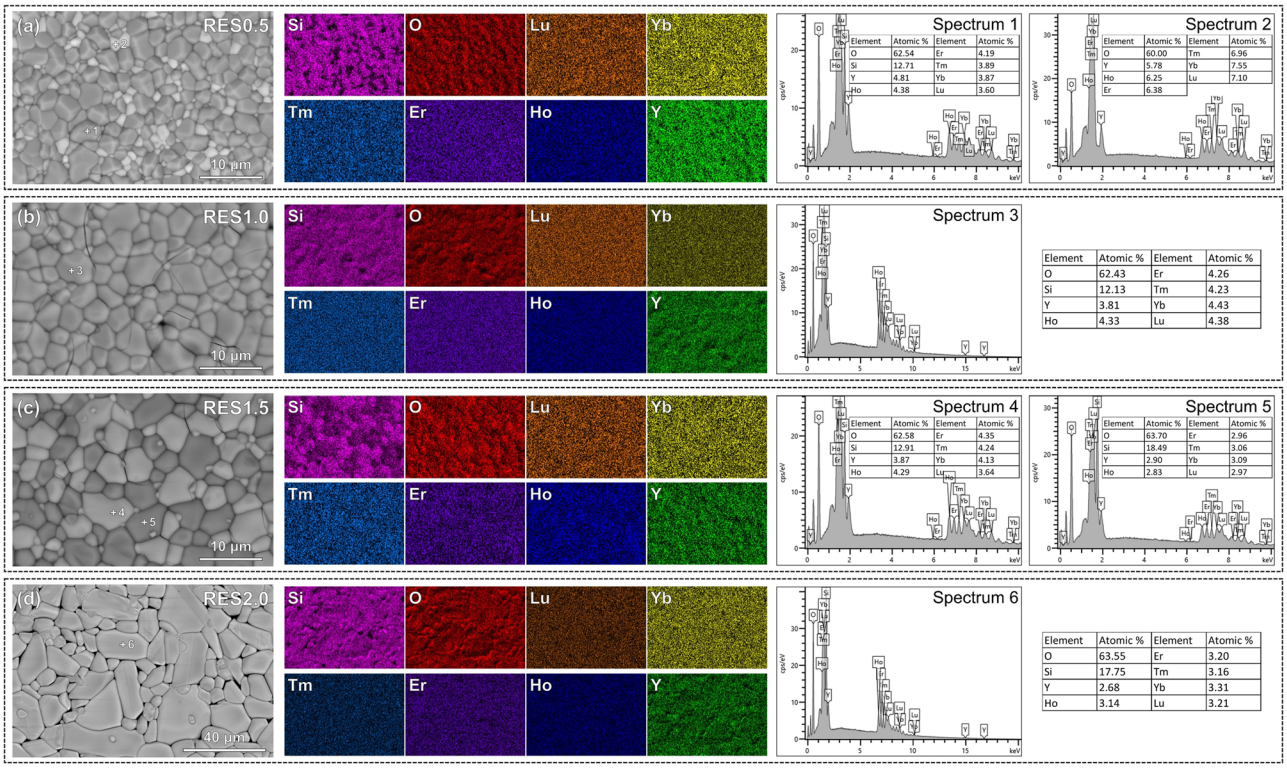

Fig. 2 | Micromorphology, EDS elemental mappings, and EDS semi-quantitative analysis of four high-entropy ceramic blocks. a RES0.5, **b** RES1.0, **c** RES1.5, **d** RES2.0.

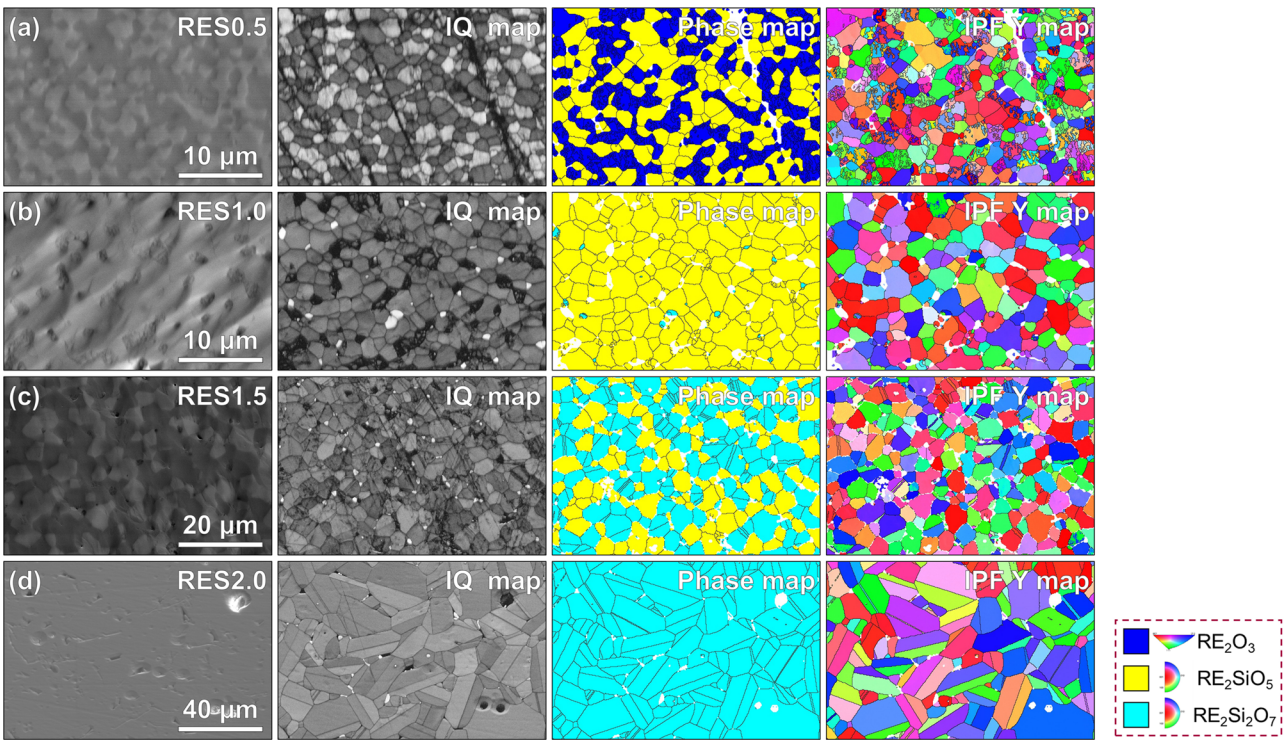

Fig. 3 | Typical EBSD datasets of polished cross-sections of four high-entropy ceramic blocks. a RES0.5, **b** RES1.0, **c** RES1.5, **d** RES2.0.

lower oxide peaks are also visible after 20 h of corrosion. Figure 5b shows the surface conditions of RES0.5 after corrosion, some residual CMAS is spread over the entire surface of the block. The cross-sectional morphologies of the RES0.5 block after corrosion are shown in Fig. 5c, d. According to the semi-quantitative EDS analysis of points 1–4 (see Fig. 5d) in Fig. 5f, it is clear that the substance (point 1) covering the top of the blocks with the darkest contrast is the residual CMAS, corresponding to the brightest part in the Si and Ca elemental mappings (see Fig. 5e). The grains (point 2) accumulated at the interface between the CMAS and the RES0.5 block are corrosion

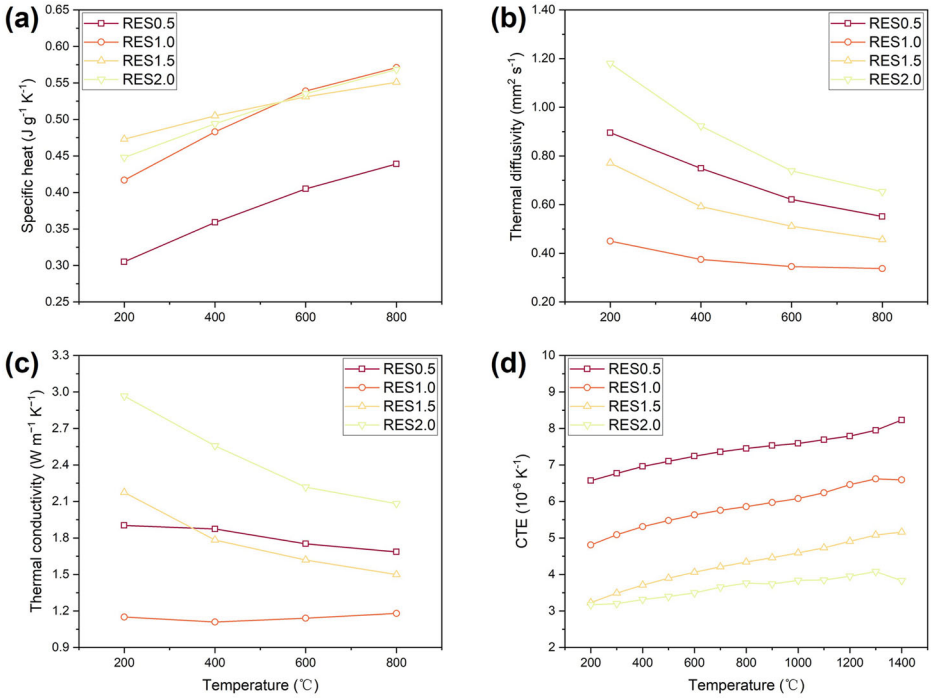

Fig. 4 | Thermophysical properties of four high-entropy ceramic blocks. a Thermal diffusivity, **b** specific heat, **c** thermal conductivity, and **d** coefficients of thermal expansion of RES0.5, RES1.0[25], RES1.5, and RES2.0[29].

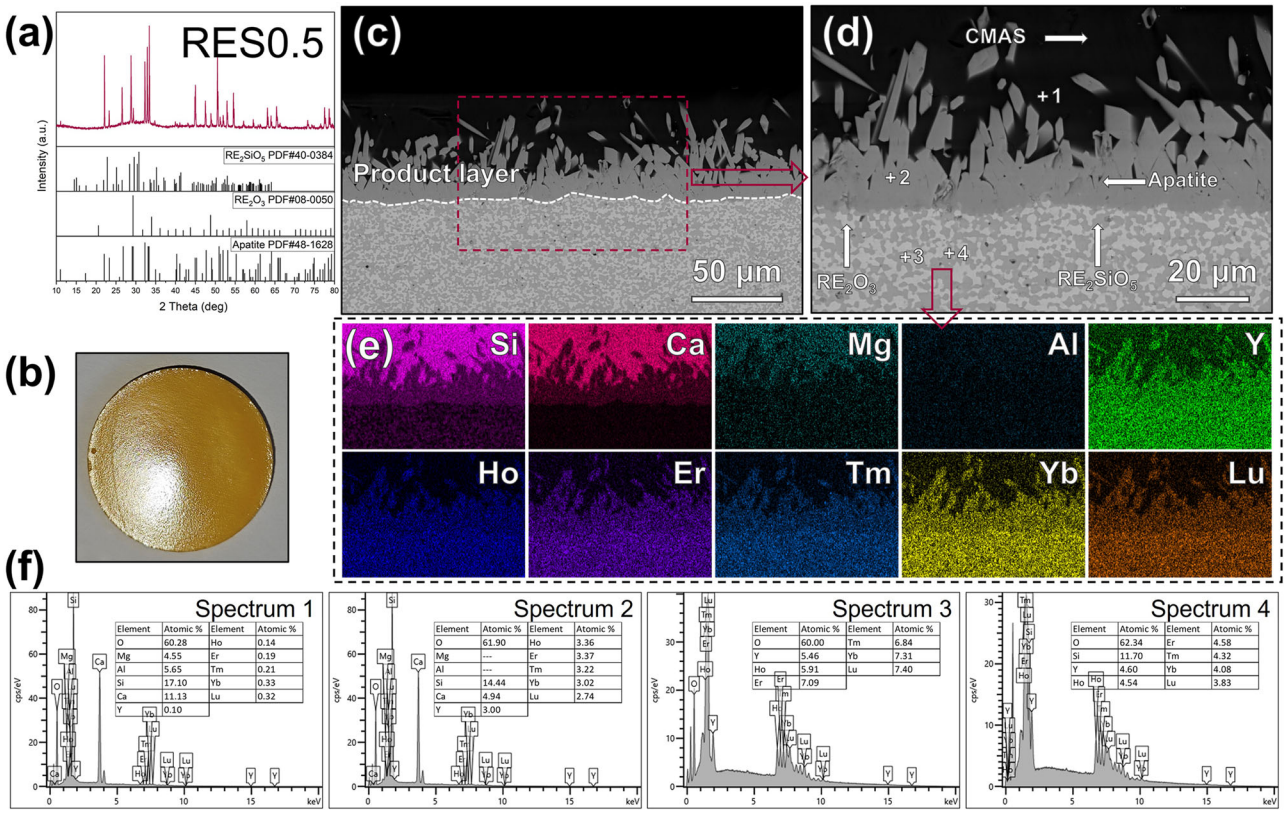

Fig. 5 | The corrosion results of RES0.5 after CMAS corrosion at 1400 °C for 20 h. a XRD pattern, **b** macro-photos, **c**, **d** SEM images of cross-section, **e** EDS elemental mappings, and **f** EDS semi-quantitative analysis.

product apatite, corresponding to the second brightest part of the Ca elemental mappings. The substances (points 3 and 4) in the brightest and second brightest contrast area at the bottom of the figure are uncorroded oxide and monosilicate. According to the cross-section of RES0.5 after corrosion (see Fig. 5c), the product layer with an average thickness of 21.8 μm consists of uniform apatite grains. The EBSD analysis (Fig. 6) indicates that the outer corrosion layer consists of apatite grains (green phase) with much larger sizes than RES0.5 grains

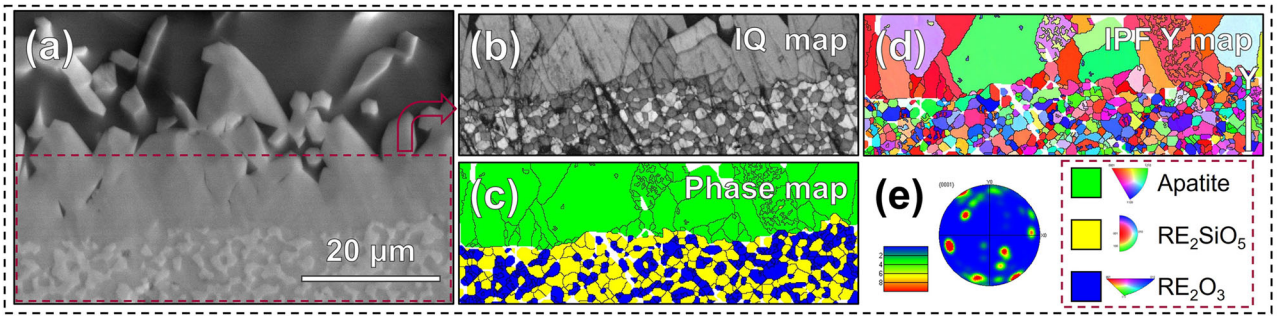

Fig. 6 | The EBSD results of RES0.5 after CMAS corrosion at 1400 °C for 20 h. a EBSD scanning area, **b** image quality map, **c** phase map, **d** IPF Y map, and **e** pole figure of apatite.

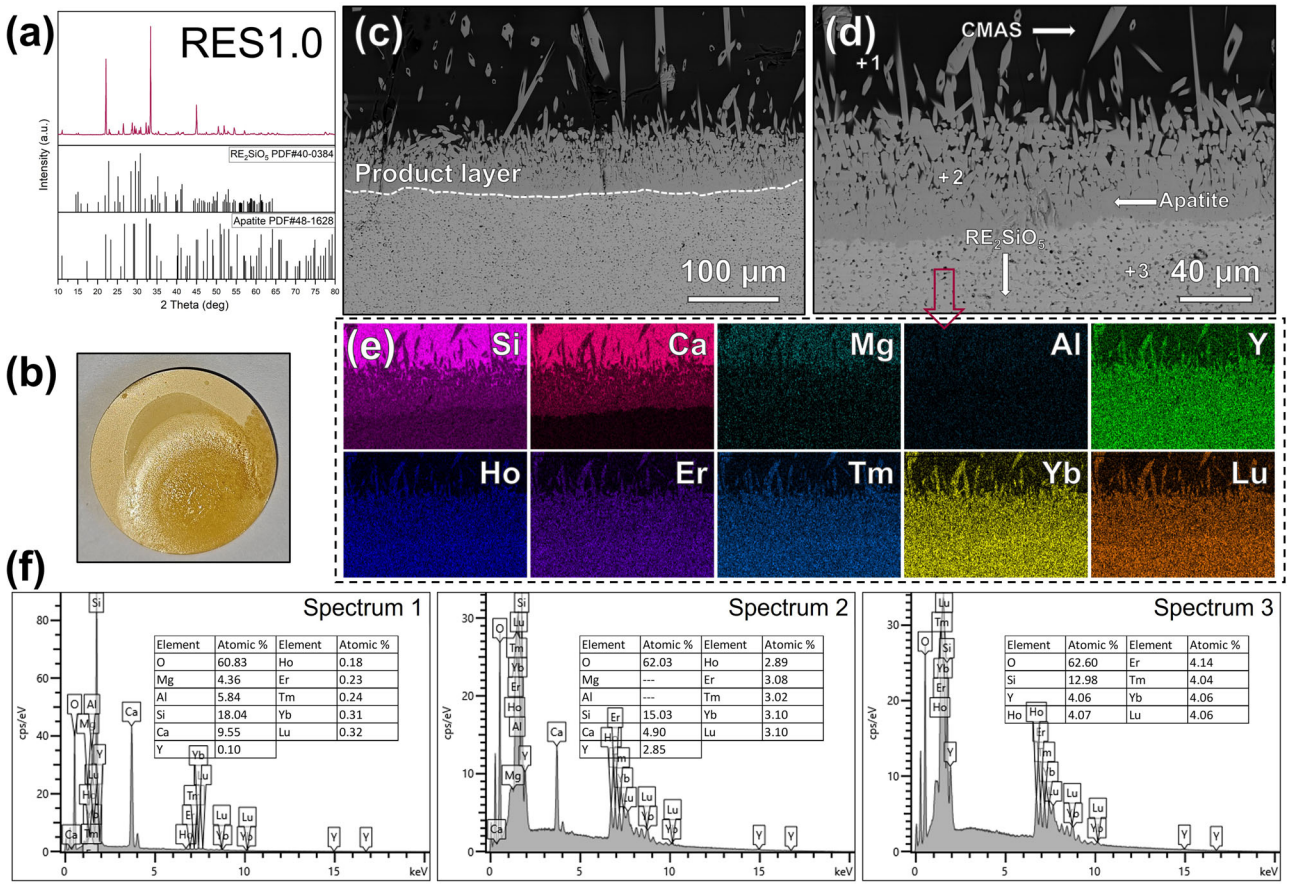

Element	Atomic %	Element	Atomic %
O	60.83	Ho	0.18
Mg	4.36	Er	0.23
Al	5.84	Tm	0.24
Si	18.04	Yb	0.31
Ca	9.55	Lu	0.32
Y	0.10		

Element	Atomic %	Element	Atomic %
O	62.03	Ho	2.89
Mg	---	Er	3.08
Al	---	Tm	3.02
Si	15.03	Yb	3.10
Ca	4.90	Lu	3.10
Y	2.85		

Element	Atomic %	Element	Atomic %
O	62.60	Er	4.14
Si	12.98	Tm	4.04
Y	4.06	Yb	4.06
Ho	4.07	Lu	4.06

Fig. 7 | The corrosion results of RES1.0 after CMAS corrosion at 1400 °C for 20 h. a XRD pattern, **b** macro-photos, **c**, **d** SEM images of cross-section, **e** EDS elemental mappings, and **f** EDS semi-quantitative analysis.

(yellow and blue phases) is continuous. All CMAS remain above the product layer and do not penetrate through the product layer into the block, and the RES0.5 block as a whole presents an uncorroded state. The IPF Y map (see Fig. 6d) and the polar figure of the apatite grain (see Fig. 6e) show that the product apatite preserved the randomly crystallographic information. The orientations refer to a coordinate system in which the Y-axis is perpendicular to the original block substrates. RES0.5, which consists of a monosilicate and oxide multiphase, demonstrates the best CMAS corrosion resistance among the four high-entropy ceramics.

The XRD pattern, surface condition, cross-sectional morphology, EDS results, and EBSD results of RES1.0 after CMAS corrosion at 1400 °C are demonstrated in Fig. 7. The strong diffraction peaks of corrosion product apatite can be seen in Fig. 7a. Unlike the previous one (RES0.5), the CMAS is concentrated on the lower right corner of the RES1.0 block surface (Fig. 7b). According to the semi-quantitative EDS analysis of points 1–3 (see Fig. 7d) in Fig. 7f, it is clear that the material (point 1) with the darkest contrast, the grains (point 2) with a dark gray contrast, and the substance (point 3) in the brightest contrast area at the bottom of the figure represent residual CMAS, apatite, and monosilicate, respectively. The EDS mappings (Fig. 7e) reflect the differences in the elemental content of different materials. The EBSD results (see Fig. 8) indicate that the product layer with an average thickness of 66.7 μm is composed of numerous fine apatite grains. Most of the red apatite grains in the IPF Y image (see Fig. 8d) and the high-intensity regions around the y-poles of the {0001} pole figure in Fig. 8e indicate a preference for apatite c-axis orientation around the substrate normal.

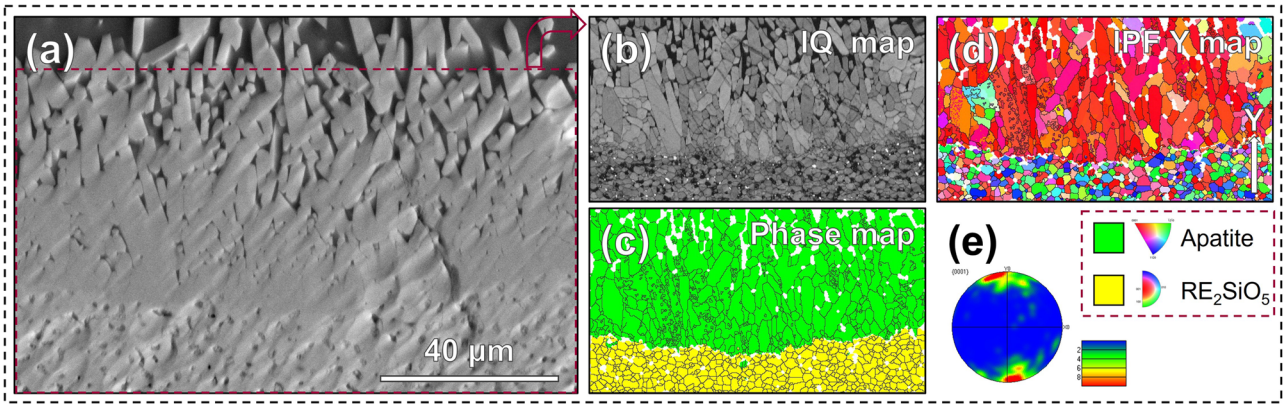

Fig. 8 | The EBSD results of RES1.0 after CMAS corrosion at 1400 °C for 20 h. a EBSD scanning area, **b** image quality map, **c** phase map, **d** IPF Y map, and **e** pole figure of apatite.

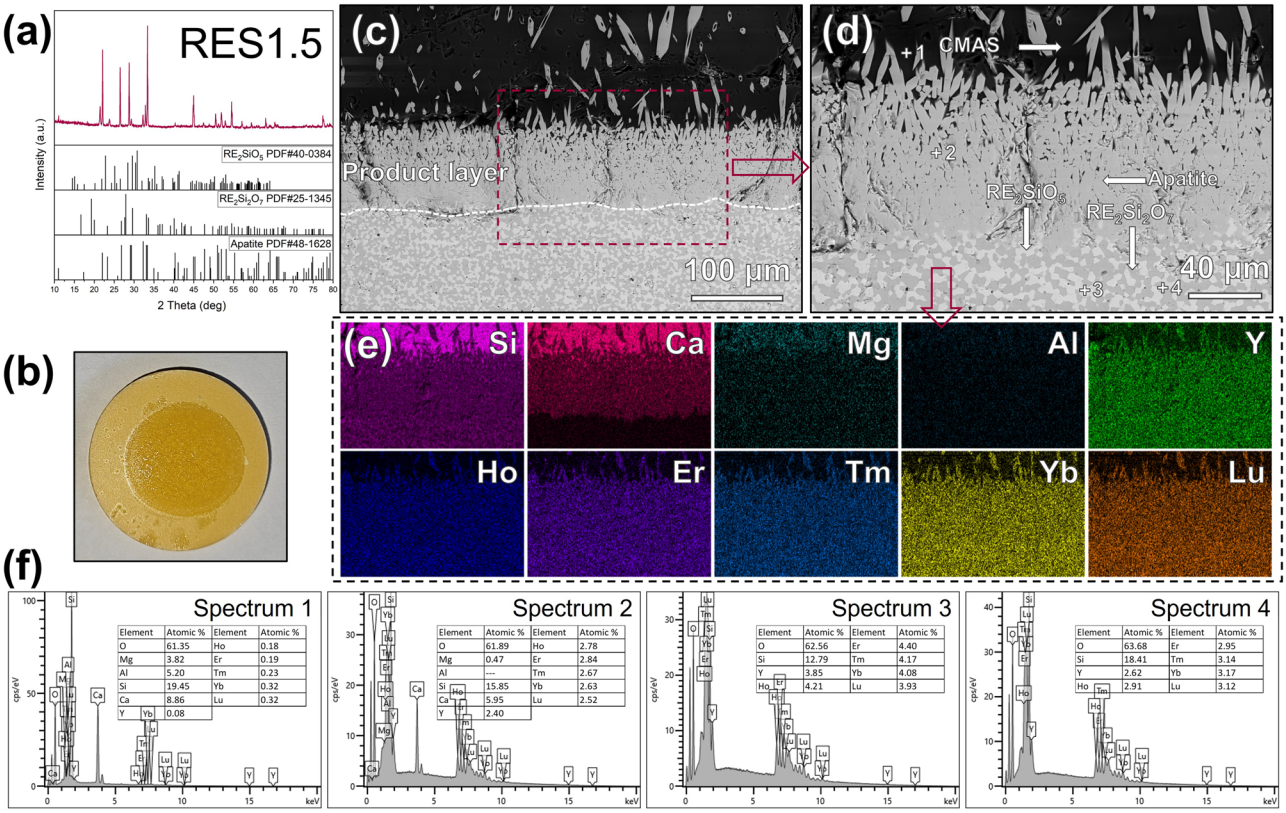

Fig. 9 | The corrosion results of RES1.5 after CMAS corrosion at 1400 °C for 20 h. a XRD pattern, **b** macro-photos, **c**, **d** SEM images of cross-section, **e** EDS elemental mappings, and **f** EDS semi-quantitative analysis.

The corrosion of the RES1.5 block at 1400 °C is illustrated in Fig. 9. The main corrosion product was also apatite (Fig. 9a), and the remaining CMAS was concentrated in the center of the block (Fig. 9b). According to the semi-quantitative EDS analysis results (see Fig. 9f), it is clear that the materials of points 1–4 in Fig. 9d are CMAS, apatite, monosilicate, and pyrosilicate, respectively. The average thickness of the product layer was 90.1 μm, which was close to RES1.0. Similar to the previous one (RES1.0), there was also a preference for the apatite crystal plane (0001) orientation over the substrate normal (see Fig. 10d, e).

Figure 11 illustrates the corrosion of RES2.0 after 20 h of CMAS corrosion at 1400 °C. As can be seen from Fig. 11a, strong diffraction peaks of corrosion product apatite and weak peaks of β-type pyrosilicate can be observed. Some of the remaining CMAS was concentrated in the center of the RES2.0 block. As can be seen from the elemental composition in Fig. 11f, the substance with dark gray contrast (point 1) shown in Fig. 11d is the CMAS molten salt, the material with light gray contrast (point 3) is pyrosilicate, and the grains (point 2) accumulated at the interface of CMAS and RES2.0 block are apatite. Figure 12 shows that although the apatite product grains are large in size and selectively oriented, unlike the case of the first three high-entropy blocks, the product layer composed of apatite is not very dense and continuous. Numerous channels between the apatite grains are permeable to CMAS, and the molten CMAS passes directly through the apatite layer and directly contacts the pyrosilicate. RES2.0 displayed the weakest corrosion resistance with an average product layer thickness of 183.0 μm, which was substantially thicker than that of RES0.5, RES1.0, and RES1.5.

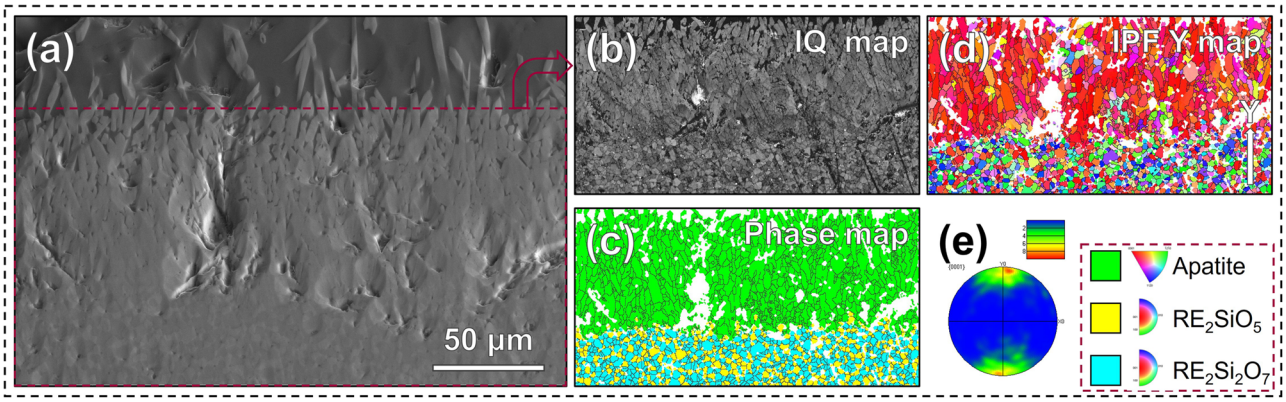

Fig. 10 | The EBSD results of RES1.5 after CMAS corrosion at 1400 °C for 20 h. a EBSD scanning area, **b** image quality map, **c** phase map, **d** IPF Y map, and **e** pole figure of apatite.

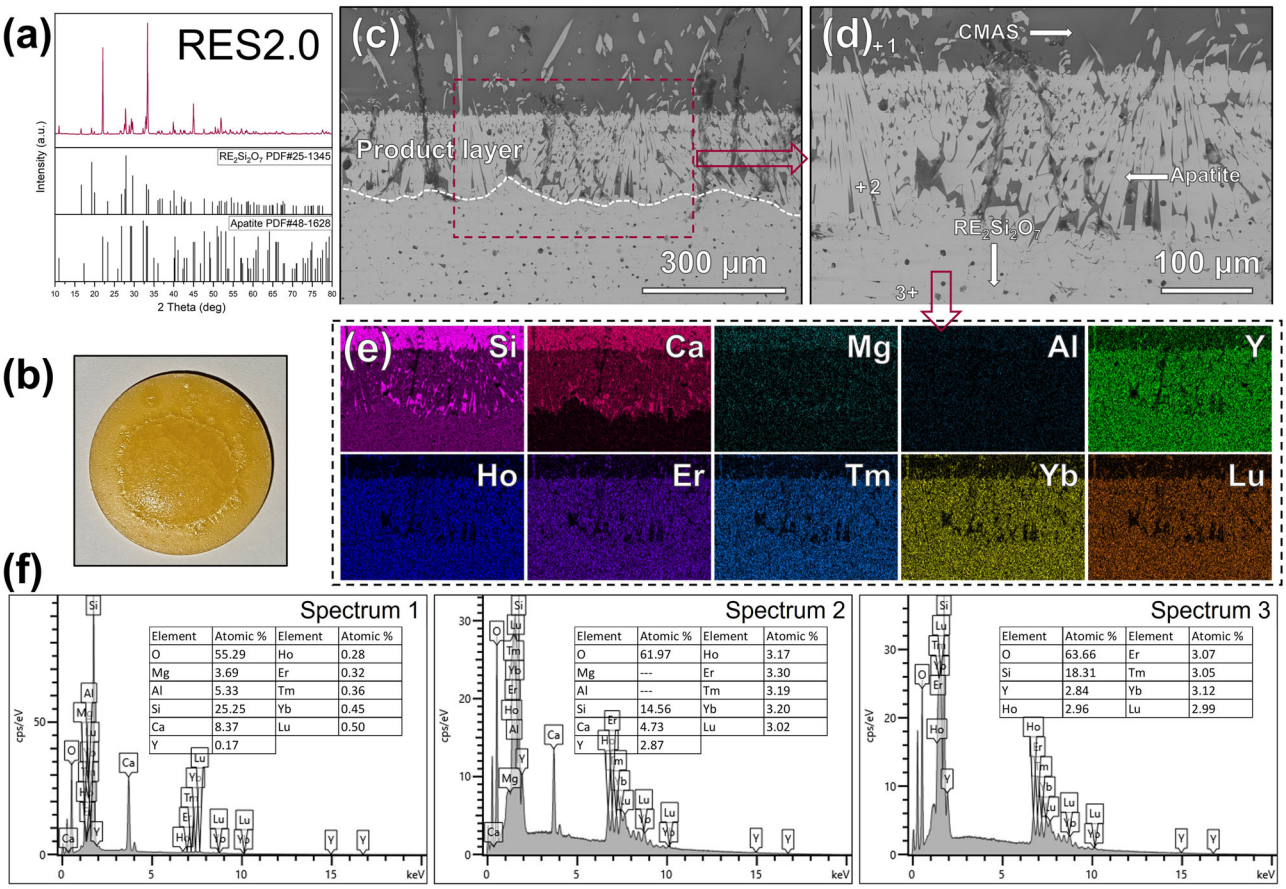

Fig. 11 | The corrosion results of RES2.0 after CMAS corrosion at 1400 °C for 20 h. a XRD pattern, **b** macro-photos, **c**, **d** SEM images of cross-section, **e** EDS elemental mappings, and **f** EDS semi-quantitative analysis.

Discussion

Since only these oxides were involved in apatite formation reactions, the ternary phase diagram of CaO-SiO_2-REO1.5 drawn by David et al. [32]. can be utilized to explain the CMAS corrosion process on RE oxides and silicates. As the four types of high-entropy ceramics are dissolved in the CMAS liquid melt, the liquid components move toward the liquid phase field. Then, all four melt components will first enter the two-phase field of apatite + liquid phase, so that the main corrosion product of all four high-entropy ceramic blocks is apatite. Even though it has been reported in some literature that RE oxides and monosilicates would form products garnet during corrosion[33], this phenomenon was not observed in this experiment.

The corrosion product, Ca:RE oxyapatite ($P6_3/m$), nominally $Ca_2RE_8(SiO_4)_6O_2$, is a defect-free apatite with a RE:Ca ratio of 4:1[34]. RE^{3+} alone occupies six cationic sites (coordinated to seven oxyanions), and the remaining cationic sites (coordinated to nine oxyanions) are occupied by Ca^{2+} and remaining RE^{3+}. The thermodynamics of the apatite formation reaction shows that the larger the radius of RE^{3+} ions, the lower the enthalpy of the formation of $Ca_2RE_8(SiO_4)_6O_2$, which suggests that the reaction would proceed more easily[35]. The four high-entropy samples all contained six different REEs (Lu, Yb, Tm, Er, Ho, and Y). Because of the difference in the enthalpy of apatite formation for different types of REEs, there are differences in the precipitation behavior of apatite crystallization in CMAS.

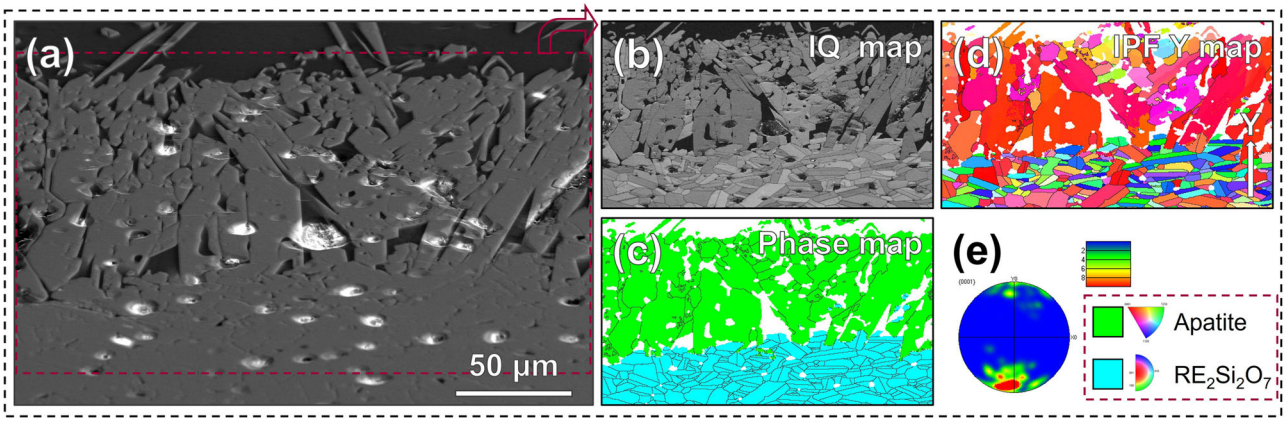

Fig. 12 | The EBSD results of RES2.0 after CMAS corrosion at 1400 °C for 20 h. a EBSD scanning area, **b** image quality map, **c** phase map, **d** IPF Y map, and **e** pole figure of apatite.

Fig. 13 | Rare earth element content in CMAS and apatite. a Atomic percentage of six RE elements in CMAS; **b** atomic percentage of six RE elements in apatite.

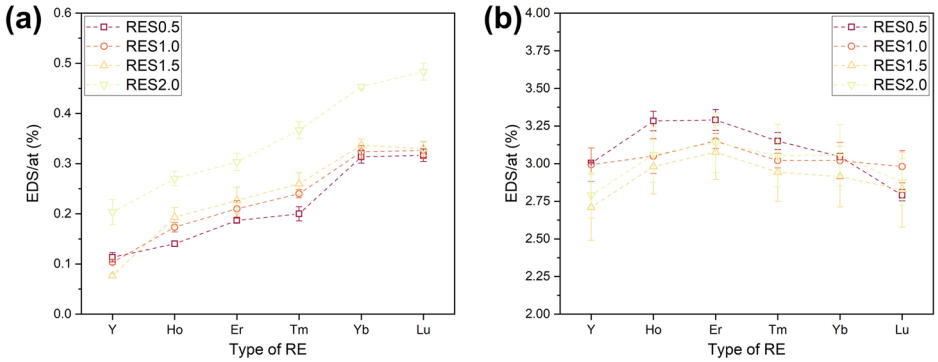

Fig. 14 | Schematics of the envisaged CMAS corrosion mechanisms and average thickness of the product layer of four high-entropy ceramic blocks. a RES0.5, **b** RES1.0, **c** RES1.5, **d** RES2.0, and **e** average thickness of the product layer.

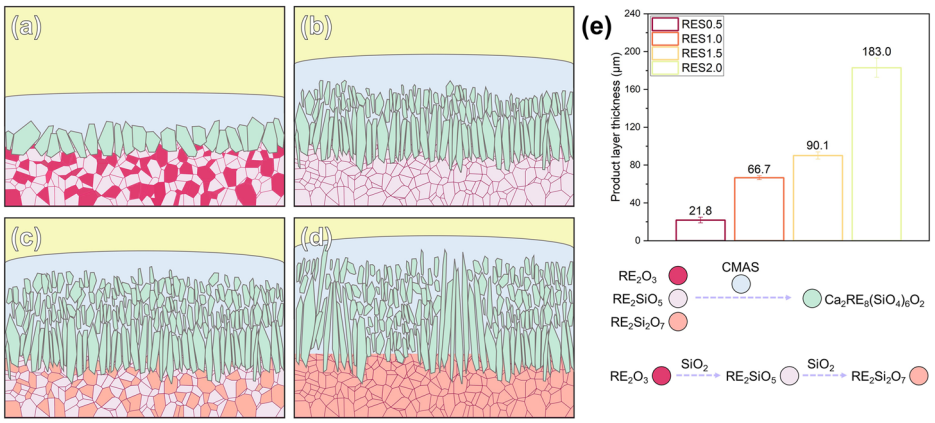

Figure 13a, b shows the contents of Lu, Yb, Tm, Er, Ho, and Y in CMAS molten salt and apatite after corrosion of four high-entropy ceramic blocks, where each data obtained from the average of three EDS semi-quantitative analyses. The EDS analysis revealed that increasing the radius of RE^{3+} leads to a gradual decrease in the content of REEs in CMAS and a gradual increase in the content of lanthanide REEs (except Y) in apatite, indicating that RE^{3+} ions with large ionic radius possess higher reactivity with CaO to form apatite from CMAS. Because the atomic number of Y element (39) is very different from the other five REE elements (67–71) and different results are obtained from the K-line series and the L-line series of Y element, the semi-quantitative EDS analysis results of Y element are not very reliable[10,11].

The diagram of the corrosion reaction of RESx high-entropy ceramics with various average product layer thicknesses is presented in Fig. 14. For all four block types, the main corrosion product is apatite, but the reactions that occur during corrosion are not the same. The chemical equations for the reaction of RE oxides, monosilicates, and pyrosilicates with CaO or SiO_2 in CMAS to form apatite are as follows:

$$4RE_2O_3 + 2CaO(CMAS) + 6SiO_2(CMAS) = Ca_2RE_8(SiO_4)_6O_2 \quad (1)$$

$$4RE_2SiO_5 + 2CaO(CMAS) + 2SiO_2(CMAS) = Ca_2RE_8(SiO_4)_6O_2 \quad (2)$$

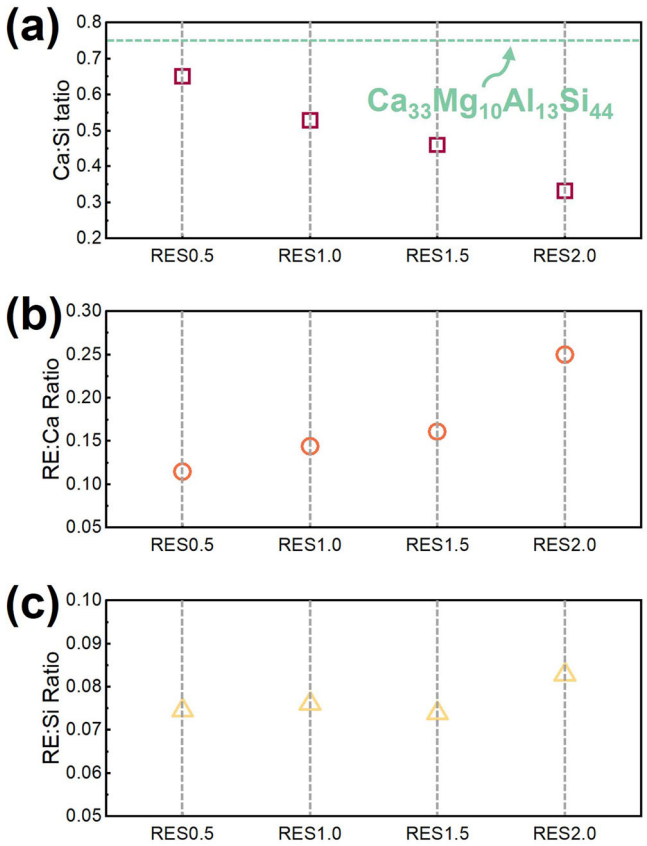

Fig. 15 | The ratios of Ca:Si, RE:Ca, and RE:Si in the residual CMAS after corrosion of four high-entropy ceramic blocks. a Ca:Si, **b** RE:Ca, and **c** RE:Si.

$$4RE_2Si_2O_7 + 2CaO(CMAS) = Ca_2RE_8\left(SiO_4\right)_6O_2 + 2SiO_2 \quad (3)$$

In addition, RE oxides and monosilicates may undergo the following intermediate reactions with SiO_2:

$$RE_2O_3 + SiO_2(CMAS) = RE_2SiO_5 \quad (4)$$

$$RE_2SiO_5 + SiO_2(CMAS) = RE_2Si_2O_7 \quad (5)$$

In general, 0.5 mol of CaO and 1.5 mol of SiO_2 in CMAS are consumed per mol of RE oxide in the corrosion reaction, both amounts being 0.5 mol for monosilicates. However, the corrosion reaction of pyrosilicates involves an equimolar exchange of CaO for SiO_2, which prevents the consumption of CMAS. The composition of the CMAS melt evolves as the composition of four types of samples, as shown in Fig. 15. According to the different consumption of CaO and SiO_2, as well as the production of SiO_2 in Eqs. (3–5), the Ca:Si ratio in the residual CMAS melt after 20 h of corrosion deviates from the initial ratio (3:4) for all four samples. The Ca:Si ratio decreases with increasing x (Si:RE ratio) in RESx due to the difference in SiO_2 consumption and production capacity of RE oxides, monosilicates, and pyrosilicates, as well as the amount of apatite produced after corrosion of the four samples. The RE:Ca ratio still grows with increasing x (Si:RE ratio) in RESx, meaning that more CaO was consumed while more REEs were diffused into the CMAS. In contrast, the change in the RE:Si ratio is not significant. As illustrated in Fig. 14, more complex reaction pathways and higher consumption of CMAS allow RE oxides and monosilicates to exhibit greater corrosion resistance compared to pyrosilicates. On the other hand, unlike the corrosion product layers of the other three blocks, the non-dense and discontinuous product layer provides more opportunities for CMAS to contact with the RES2.0 (pyrosilicate) block.

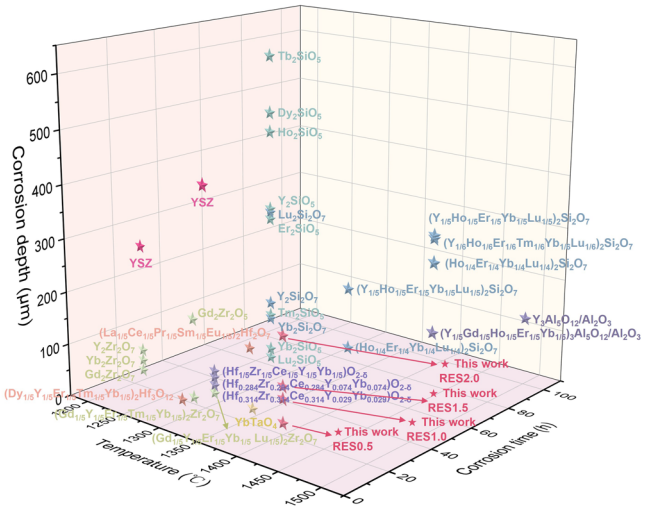

Fig. 16 | Summary of recently reported representative data, as well as data from this study, on the corrosion depth of EBC/TBC materials against molten CMAS[10,11,36–46].

Some potential EBC or thermal barrier coating (TBC) materials for CMAS corrosion resistance are shown in Fig. 16[10,11,36–46]. The thickness of corrosion products is a measure of the material's resistance to CMAS, where CMAS does not penetrate into coating material, a thinner corrosion layer means less material consumption. Rare earth materials like zirconate[36–38], monosilicates[39], tantalate[40], hafnate[41,42], and oxide[43] exhibit superior performance as coating materials compared with traditional TBC materials, yttria-stabilized zirconia (YSZ), at 1300–1350 °C. However, the surface temperature of EBCs may increase to 1400 °C. After exposure to corrosion at å 1400 °C, the corrosion depths of high-entropy rare earth pyrosilicates[10,11,44] and $RE_3Al_5O_{12}/Al_2O_3$ multiphase material[45,46] still exceeded 100 μm. The two types of high-entropy multiphase coating materials from this study exhibited excellent corrosion resistance at 1400 °C, especially RES0.5, whose corrosion depth was only 21.8 μm after 20 h of corrosion.

Compared to RES1.0 (pure high-entropy monosilicate phase), the pyrosilicate phase in RES1.5 more importantly serves to reduce the coefficient of thermal expansion, and, giving RES1.5 close CMAS corrosion resistance compared to RES1.0, while having a better-matched coefficient of thermal expansion to SiC_f/SiC[28]. The multiphase structure design balances the advantages and disadvantages of the properties of monosilicates and pyrosilicates, giving RES1.5 a superior all-around performance as an EBC material for application on SiC_f/SiC CMC. RES0.5 exhibits the best CMAS corrosion resistance among the four high-entropy ceramics. The monosilicate phase, on the one hand, reduces the thermal conductivity of the block as a whole, making the thermal conductivity of this multiphase material much lower than that of the RE oxides[13]. On the other hand, it allows RES0.5 to achieve a slightly lower coefficient of thermal expansion than that of Al_2O_{3f}/Al_2O_3[17], during the thermal cycling process, the coating made from it can only be subjected to compressive stress, which is better for long-term service of ceramic coating. High-entropy RES0.5 multiphase ceramics that combine low thermal conductivity, a slightly lower coefficient of thermal expansion than Al_2O_{3f}/Al_2O_3, and excellent CMAS corrosion resistance have great potential for use in Al_2O_{3f}/Al_2O_3 CMC as an environmental barrier coating material.

In the present investigation, two types of high-entropy multiphase ceramics, RE_2SiO_5/RE_2O_3 and $RE_2SiO_5/RE_2Si_2O_7$ (RE = Lu, Yb, Tm, Er, Ho, and Y), as well as two types of high-entropy single-phase silicates (RE_2SiO_5 and $RE_2Si_2O_7$), were methodically synthesized by the solid-phase method. The thermal performance and CMAS corrosion resistance at 1,400 °C of four pyrosilicates were appropriately tested:

1. The phase compositions of four types of high-entropy ceramics (RES0.5–RES1.0–RES1.5–RES2.0) undergo the following transformations: RE_2SiO_5/RE_2O_3–RE_2SiO_5–$RE_2SiO_5/RE_2Si_2O_7$–$RE_2Si_2O_7$. The grains of different phases with various sizes bonded tightly together to form dense blocks of multiphase RES0.5 and RES1.5. High-entropy monosilicates in RES0.5, RES1.0, and RES1.5 were found to exist in the X2-type, and high-entropy pyrosilicates in RES1.5 and RES2.0 were found to exist in the β phase.
2. The measured coefficient of thermal expansion and thermal conductivity values of two types of multiphase ceramics largely agree with the rule of mixtures. The CTE and conductivity of RES0.5 is between those of rare earth oxide and RES1.0, while the CTE and conductivity of RES1.5 is between those of RES1.0 and RES2.0. Due to the presence of 50% of the six-component monosilicate phase in RES0.5 and RES1.5, they have significantly lower thermal conductivity. The CTE of RES1.5 is $3.23–5.16 \times 10^{-6}\ K^{-1}$, which is close to and slightly lower than that of SiC_f/SiC. The CTE of another high-entropy multiphase ceramic—RES0.5 is $6.57–8.23 \times 10^{-6}\ K^{-1}$, which is also slightly lower than that of Al_2O_{3f}/Al_2O_3.
3. In CMAS corrosion testing, RES0.5 showed the strongest corrosion resistance due to more complex reaction pathways and higher CMAS consumption. The corrosion resistance of RES1.5 is also significantly better than that of pure phase pyrosilicates.

RES0.5 and RES1.5 combine the advantages of high-entropy RE oxide with monosilicate and monosilicate with pyrosilicate, respectively, with low thermal conductivity, coefficients of thermal expansion consistent with those of CMCs, and excellent CMAS corrosion resistance, having a great potential to be used as environmental barrier coatings.

Methods

Material synthesis

Two high-entropy multiphase ceramics—RE_2SiO_5/RE_2O_3 (RES0.5) and $RE_2SiO_5/RE_2Si_2O_7$ (RES1.5) (where RE = Lu, Yb, Tm, Er, Ho, and Y), one high-entropy monosilicate (RES1.0), and a type of high-entropy pyrosilicate (RES2.0) were prepared by a solid-phase methodology. RE_2O_3 (RE = Lu, Yb, Tm, Er, Ho, and Y) and SiO_2 powders were utilized as the starting materials. The molar ratio of each RE_2O_3 was equal, and the total molar ratios of RE_2O_3 to SiO_2 were 0.5, 1.0, 1.5, and 2.0 for RES0.5, RES1.0, RES1.5, and RES2.0, respectively. The powder container was homogeneously mixed in a vertical nylon tank by a ball mill using ethanol and zirconia balls as the dispersion medium. The resulting slurry was then dried at 120 °C for 5 h and then passed through a sieve. The powder was placed under the sieve in circular molds with a diameter of 15 mm and 20 mm and then cold pressed into the required shape. After cold pressing, the green billets were placed in a muffle furnace and kept at 1500 °C for 5 h and 1700 °C for 10 h to obtain high-entropy ceramic blocks. The CMAS powders with the chemical formula $Ca_{33}Mg_{10}Al_{13}Si_{44}$ were appropriately synthesized by similar processes from CaO, MgO, Al_2O_3, and SiO_2 powders[10]. The mixed powders were kept in a muffle furnace at 1400 °C for 5 h to obtain CMAS glass, and CMAS powders were suitably derived by grinding CMAS glass.

CMAS corrosion

The surfaces of the blocks to be corroded were coated with the CMAS powders to obtain a concentration of 25 mg/cm^2. Then, the blocks coated with CMAS powders were transferred to a muffle furnace and held at 1400 °C for 20 h.

Characterization

An X-ray diffraction approach (XRD, D8 ADVANCE, Bruker, Germany) was employed to determine the phase composition of four types of high-entropy ceramics before and after corrosion. The X-ray power was 40 kV and 40 mA; a 0.6 mm evanescent slit was used for data collection. Data were recorded over 2θ range of 10°–110° with a 0.8°/min and 10°–80° with a 10°/min. The results of XRD analysis were refined via FullProf software to obtain the lattice parameters and atomic occupancy of two types of multiphase ceramics. We also used scanning electron microscopy (SEM, Magellan 400, FEI, USA) equipped with an energy-dispersive X-ray spectrometer (EDS, Oxford, England) and an electron backscatter diffraction (EBSD, Oxford, England) attachment to comprehensively analyze the micromorphology, chemical composition, and orientation information of high-entropy ceramic blocks before and after corrosion. The density (ρ) was measured by the Archimedean drainage method. The thermal diffusivity (α) of the samples was measured in the temperature range of 200–800 °C using a thermal dilatometer (LFA467, NETZSCH, Germany). The heat capacity (C_p) of high-entropy ceramics was determined using a high-temperature specific heat tester (MHTC96, SETARAM, France). Then, the experimental thermal conductivity (k) of the samples was calculated based on the following relation:

$$k = \alpha C_p \rho \tag{6}$$

The coefficients of thermal expansion of two types of multiphase ceramics were measured using a thermal dilatometer (DIL 402SE, NETZSCH, Germany) from room temperature to 1400 °C with a heating rate of 10°C/min. The coefficient of thermal expansion can be calculated using the following equation:

$$CTE = \frac{\Delta L/L}{\Delta T} \tag{7}$$

Where L, ΔL, and ΔT represent the length of the sample at room temperature, the change in the length, the temperature difference, respectively.

Data availability

All research data supporting this publication are directly available within this publication.

Received: 18 December 2023; Accepted: 15 March 2024;
Published online: 10 April 2024

References

1. Padture, N. P. Advanced structural ceramics in aerospace propulsion. *Nat. Mater.* **15**, 804–809 (2016).
2. Deijkers, J. A. & Wadley, H. A duplex bond coat approach to environmental barrier coating systems. *Acta Mater.* **217**, 117167 (2021).
3. Chen, Z. et al. $(Ho_{0.25}Lu_{0.25}Yb_{0.25}Eu_{0.25})_2SiO_5$ high-entropy ceramic with low thermal conductivity, tunable thermal expansion coefficient, and excellent resistance to CMAS corrosion. *J. Adv. Ceram.* **11**, 1279–1293 (2022).
4. Naslain, R. Recent advances in the field of ceramic fibers and ceramic matrix composites. *J. Phys. IV Fr.* **123**, 3–17 (2005).
5. Igawa, N. et al. Fabrication of SiC fiber reinforced SiC composite by chemical vapor infiltration for excellent mechanical properties. *J. Phys. Chem. Solids* **66**, 551–554 (2005).
6. Naslain, R. Design, preparation and properties of non-oxide CMCs for application in engines and nuclear reactors: an overview. *Compos Sci. Technol.* **64**, 155–170 (2004).
7. Chen, Z. et al. Water vapor corrosion behaviors of high-entropy pyrosilicates. *J. Materiomics* **8**, 992–1000 (2022).
8. Eaton, H. & Linsey, G. Accelerated oxidation of SiCCMC's by water vapor and protection via environmental barrier coating approach. *J. Eur. Ceram. Soc.* **22**, 2741–2747 (2022).
9. Opila E., Myers D., Alumina volatility in water vapor at elevated temperatures: Application to combustion environments, High Temperature Corrosion and Materials Chemistry IV, pp. 535–544 (2003).

10. Chen, Z., Lin, C., Zheng, W., Zeng, Y. & Niu, Y. Investigation on improving corrosion resistance of rare earth pyrosilicates by high-entropy design with RE-doping. *Corros. Sci.* **199**, 110217 (2022).
11. Chen, Z. et al. Mechanism of enhanced corrosion resistance against molten CMAS for pyrosilicates by high-entropy design. *J. Am. Ceram. Soc.* **106**, 6000–6013 (2023).
12. Chen, Z. et al. A high-entropy $(Yb_{0.2}Y_{0.2}Lu_{0.2}Ho_{0.2}Er_{0.2})_2Si_2O_7$ environmental barrier coating prepared by atmospheric plasma-spray. *Ceram. Int* **49**, 11323–11333 (2023).
13. Sun, Y. et al. Preparation and properties of CMAS resistant bixbyite structured high-entropy oxides RE_2O_3 (RE = Sm, Eu, Er, Lu, Y, and Yb): Promising environmental barrier coating materials for Al_2O_{3f}/Al_2O_3. *Compos., J. Adv. Ceram.* **10**, 596–613 (2021).
14. Wu, P. & Pelton, A. Coupled Thermodynamic—Phase Diagram Assessment of the Rare Earth Oxide–Aluminum Oxide Binary System. *J. Alloy Compd.* **179**, 259–287 (1992).
15. Nielsen, T. & Leipold, M. Thermal Thermal Expansion of Yttrium Oxide and Magnesium Oxide with Yttrium Oxide. *J. Am. Ceram. Soc.* **47**, 256–256 (1964).
16. Curtis, C. Properties of Yttrium Oxide Ceramics. *J. Am. Ceram. Soc.* **40**, 274–278 (1957).
17. Gatzen, C., Mack, D., Guillon, O. & Vaßen, R. $YAlO_3$-A Novel Environmental Barrier Coating for Al_2O_3/Al_2O_3-Ceramic Matrix Composites. *Coatings* **9**, 609 (2019).
18. Eils, N., Mechnich, P. & Braue, W. Effect of CMAS Deposits on MOCVD Coatings in the System Y_2O_3-ZrO_2: Phase Relationships. *J. Am. Ceram. Soc.* **96**, 3333–3340 (2013).
19. Ping, X. et al. Structural, mechanical and thermal properties of cubic bixbyite-structured high-entropy oxides. *Chem. Eng. J.* **464**, 142649 (2023).
20. Li, M. et al. Order-disorder transition and thermal conductivities of the $(NdSmEuGd)_{(1-x)/2}Dy_{2x}Zr_2O_7$ series. *J. Materiomics* **9**, 138–147 (2023).
21. Liao, W. et al. High entropy $(Y_{1/5}Ho_{1/5}Er_{1/5}Yb_{1/5}Lu_{1/5})_3Al_5O_{12}$ with low thermal conductivity and high thermal stability. *J. Alloy Compd.* **949**, 169736 (2023).
22. Zhao, Z. et al. High-entropy $(Nd_{0.2}Sm_{0.2}Eu_{0.2}Y_{0.2}Yb_{0.2})_4Al_2O_9$ with good high temperature stability, low thermal conductivity, and anisotropic thermal expansivity. *J. Adv. Ceram.* **9**, 595–605 (2020).
23. Zhang, P. et al. Xenotime-type high-entropy $(Dy_{1/7}Ho_{1/7}Er_{1/7}Tm_{1/7}Yb_{1/7}Lu_{1/7}Y_{1/7})PO_4$: A promising thermal/environmental barrier coating material for SiC_f/SiC ceramic matrix composites. *J. Adv. Ceram.* **12**, 1033–1045 (2023).
24. Zhang, P. et al. Preparation and characterization of a novel monazite-type high-entropy $(La_{1/7}Ce_{1/7}Pr_{1/7}Nd_{1/7}Sm_{1/7}Eu_{1/7}Gd_{1/7})PO_4$ for thermal/environmental barrier coatings. *J. Alloy Compd.* **952**, 169978 (2023).
25. Chen, Z. et al. High-entropy engineering promotes the thermal properties of monosilicates. *J. Eur. Ceram. Soc.* **44**, 1217–1228 (2024).
26. Liu, P. et al. Reaction behaviors and mechanisms of tri-layer Yb_2SiO_5/$Yb_2Si_2O_7$/Si environmental barrier coatings with molten calcium-magnesium-alumino-silicate. *Corros. Sci.* **197**, 110069 (2022).
27. Tian, Z. et al. Theoretical and experimental determination of the major thermo-mechanical properties of RE_2SiO_5 (RE = Tb, Dy, Ho, Er, Tm, Yb, Lu, and Y) for environmental and thermal barrier coating applications. *J. Eur. Ceram. Soc.* **36**, 189–202 (2016).
28. Lee, K., Eldridge, J. & Robinson, R. Residual stresses and their effects on the durability of environmental barrier coatings for SiC ceramics. *J. Am. Ceram. Soc.* **88**, 3483–3488 (2005).
29. Chen, Z. et al. Influence of average radii of RE^{3+} ions on phase structures and thermal expansion coefficients of high-entropy pyrosilicates. *J. Adv. Ceram.* **12**, 1–15 (2023).
30. Zhong, X. et al. Thermal shock resistance of tri-layer Yb_2SiO_5/$Yb_2Si_2O_7$/Si coating for SiC and SiC-matrix composites. *J. Am. Ceram. Soc.* **101**, 4743–4752 (2018).
31. Zhong, X. et al. Thermal Shock Resistance of Yb_2SiO_5/Si and $Yb_2Si_2O_7$/Si Coatings Deposited on C/SiC Composites. *Solid State Phenom.* **281**, 472–477 (2018).
32. Poerschke, D. et al. Phase equilibria and crystal chemistry in the calcia-silica-yttria system. *J. Eur. Ceram. Soc.* **36**, 1743–1754 (2018).
33. Zhong, X. et al. Corrosion behaviors and mechanisms of ytterbium silicate environmental barrier coatings by molten calcium-magnesium-alumino-silicate melts. *Corros. Sci.* **191**, 109718 (2021).
34. Wanmaker, W. Luminescence of alkaline earth yttrium and lanthanum phosphate-silicates with apatite structure. *J. Solid State Chem.* **3**, 452–457 (1971).
35. Costa, G. et al. Thermochemistry of calcium rare-earth silicate oxyapatites. *J. Am. Ceram. Soc.* **103**, 1446–1453 (2019).
36. Drexler, J., Ortiz, A. & Padture, N. Composition effects of thermal barrier coating ceramics on their interaction with molten Ca–Mg–Al–silicate (CMAS) glass. *Acta Mater.* **60**, 5437–5447 (2012).
37. Yan, R. et al. Mechanical, thermal and CMAS resistance properties of high-entropy $(Gd_{0.2}Y_{0.2}Er_{0.2}Tm_{0.2}Yb_{0.2})_2Zr_2O_7$ ceramics. *Ceram. Int* **49**, 20729–20741 (2023).
38. Deng, S. et al. Calcium-magnesium-alumina-silicate (CMAS) resistant high entropy ceramic $(Y_{0.2}Gd_{0.2}Er0_{.2}Yb_{0.2}Lu_{0.2})_2Zr_2O_7$ for thermal barrier coatings. *J. Mater. Sci. Technol.* **107**, 259–265 (2022).
39. Tian, Z. et al. General trend on the phase stability and corrosion resistance of rare earth monosilicates to molten calcium magnesium aluminosilicate at 1300 degrees C. *Corros. Sci.* **148**, 281–292 (2019).
40. Yang, W. & Ye, F. The thermophysical properties and the molten CMAS resistance performance of Ytterbium Tantalate. *Surf. Coat. Tech.* **423**, 127584 (2021).
41. Ye, F. et al. The CMAS corrosion behavior of high-entropy $(Y_{0.2}Dy_{0.2}Er_{0.2}Tm_{0.2}Yb_{0.2})_4Hf_3O_{12}$ hafnate material prepared by ultrafast high-temperature sintering (UHS). *J. Eur. Ceram. Soc.* **43**, 2185–2195 (2023).
42. Cong, L. et al. Hot corrosion of high-entropy hafnate for thermal barrier coating material subjected to molten CMAS. *Corros. Sci.* **209**, 110714 (2022).
43. Cheng, F. et al. Fluorite-pyrochlore structured high-entropy oxides: Tuning the ratio of B-site cations for resistance to CMAS corrosion. *Corros. Sci.* **218**, 111199 (2023).
44. Tian, Z. et al. Corrosion of $RE_2Si_2O_7$ (RE=Y, Yb, and Lu) environmental barrier coating materials by molten calcium-magnesium-alumino-silicate glass at high temperatures. *J. Eur. Ceram. Soc.* **39**, 4245–4254 (2019).
45. Sun, H. et al. Outstanding molten calcium–magnesium–aluminosilicate (CMAS) corrosion resistance of directionally solidified $Al_2O_3/Y_3Al_5O_{12}$ eutectic ceramic at 1500 °C. *Corros. Sci.* **220**, 111289 (2023).
46. Zhou, C. et al. Excellent calcium-magnesium-aluminosilicate corrosion resistance of high-entropy garnet/alumina directionally solidified eutectic at 1500 °C. *J. Am. Ceram. Soc.* **107**, 1748–1759 (2023).

Acknowledgements

This work is supported by the National Key Research and Development Program of China (2023YFF0719800).

Author contributions

Zeyu Chen (Conceptualization; Data curation; Investigation; Methodology; Visualization; Writing–original draft); Yongzhe Wang (Conceptualization; Methodology; Validation; Writing–review & editing); Yiling Huang (Data curation; Validation); Fan Peng (Conceptualization; Resources); Chucheng

Lin (Validation; Visualization); Wei Zheng (Conceptualization; Validation); Xuemei Song (Data curation; Methodology); Yaran Niu (Methodology; Supervision); Yi Zeng (Conceptualization; Project administration; Supervision; Writing–review & editing).

Competing interests

The authors declare no competing interests.

Additional information

Correspondence and requests for materials should be addressed to Yongzhe Wang or Yi Zeng.

Reprints and permissions information is available at http://www.nature.com/reprints

Publisher's note Springer Nature remains neutral with regard to jurisdictional claims in published maps and institutional affiliations.